

Distance-Aware Precoding for Near-Field Capacity Improvement

Zidong Wu, *Student Member, IEEE*, Mingyao Cui, *Student Member, IEEE*, Zijian Zhang, *Student Member, IEEE*, Linglong Dai, *Fellow, IEEE*

Abstract—Extremely large-scale MIMO (XL-MIMO) is a promising technology to improve the capacity for future 6G networks. With a very large number of antennas, the near-field property of XL-MIMO systems becomes dominant. Unlike the classical far-field line-of-sight (LoS) channel with only one available data stream, the significantly increased degrees of freedom (DoFs) are available in the near-field LoS channel. However, limited by the small number of radio frequency (RF) chains, the existing hybrid precoding architecture widely used for 5G is not able to fully exploit the extra DoFs in the near-field region. In this paper, the available DoFs and the capacity of the near-field LoS channel are theoretically analyzed at first. Then, to exploit the near-field effect as a new possibility for capacity improvement, the distance-aware precoding (DAP) scheme is proposed. We develop the DAP architecture, where a dedicated selection circuit is inserted to connect phase shifters and RF chains. Moreover, each RF chain can be flexibly configured to active or inactive according to the distance-related DoFs in the proposed DAP architecture. Based on the developed DAP architecture, a DAP algorithm is proposed to optimize the number of activated RF chains and precoding matrices to match the increased DoFs in the near-field region. Finally, simulation results verify that, the proposed DAP scheme can efficiently utilize the extra DoFs in the near-field region to improve the spectrum efficiency and the energy efficiency as well.

Index Terms—Extremely large-scale MIMO (XL-MIMO), hybrid precoding, near-field, spectrum efficiency, energy efficiency.

I. INTRODUCTION

Due to the explosively growing demand for communication capacity, spatial multiplexing is regarded as a key technology to significantly increase the spectrum efficiency [1]. By exploiting the spatial degrees of freedom (DoFs) with spatial multiplexing, massive multiple-input multiple-output (MIMO) is the key enabler to increase the capacity by orders of magnitude for 5G. To further exploit the promising potential of spatial DoFs, massive MIMO for 5G is evolving to extremely large-scale MIMO (XL-MIMO) for future 6G communications [2].

The evolution from massive MIMO to XL-MIMO not only implies a significant increase in the number of antennas, but also leads to a fundamental change of the characteristics in the electromagnetic field. Specifically, since the number of antennas of massive MIMO systems is usually not very large, the classical *far-field* MIMO channel model is widely adopted,

which is based on planar wave assumptions [3]. By contrast, with the dramatically increasing number of antennas in XL-MIMO communication systems, receivers may lie in the *near-field* region of the transmitter, which is defined by the area within the Rayleigh distance [4]. For example, if we consider an XL-MIMO system with 1000 linear antennas with half wavelength spacing, the Rayleigh distance reaches 500 m at 300 GHz, which covers a large area of a standard cell. Unlike the classical *far-field* channel based on planar wave assumptions, the *near-field* channel should be modeled based on spherical wave assumptions in XL-MIMO communications, leading to significant near-field effect [5]. Thus, traditional far-field transmission techniques may suffer from a severe performance loss due to the mismatch between *far-field* assumptions and *near-field* channel property.

A. Prior Works

Most of existing works on near-field communications focus on overcoming the performance degradation caused by the near-field effect [5]–[7]. To be specific, the steering beams are only related to the user angles under the planar wave assumptions. By contrast, due to the property of spherical waves, the beams are related to both the user angle and distance [6]. The initial work [7] has studied the near-field beamforming techniques by designing the angle- and distance-dependent beams for narrow-band communications. To achieve the near-field beamforming in wideband systems, by exploiting the varied spherical wavefronts at different frequencies, a phase-delay focusing method was proposed in [5].

To acquire high-gain beamforming, channel estimation is essential for XL-MIMO communications. Several works [8]–[11] have studied how to overcome the performance loss of channel estimation in the near-field region. In [8], a near-field channel estimation method was proposed to capture the sparsity in the joint angle-distance (polar) domain caused by spherical waves. Moreover, a more realistic hybrid-field channel model characterizing both far-field and near-field paths was investigated in [10], and the corresponding channel estimation method was also proposed. Existing works on near-field communications indicate that the near-field effect only induces performance degradation for wireless communications which is caused by the mismatch of the near-field channel model and classical far-field-based beamforming or channel estimation methods in the physical layer.

Nevertheless, the recently developed electromagnetic information theory (EIT) indicates that, wireless communications

All authors are with the Beijing National Research Center for Information Science and Technology (BNRist) as well as the Department of Electronic Engineering, Tsinghua University, Beijing 100084, China (e-mails: {wuzd19, cmy20, zhangzj20}@mails.tsinghua.edu.cn, daill@tsinghua.edu.cn).

can also benefit from the near-field effect [12]. Specifically, for far-field channels, due to the high attenuation of millimeter-wave and terahertz bands, the rank-one line-of-sight (LoS) path becomes predominant in the XL-MIMO channels, so only very limited spatial multiplexing gain can be achieved [13]. Compared with the far-field LoS path with *planar* wavefronts determined by a single spatial angle, the near-field LoS path with *spherical* wavefronts contains a range of angles, which brings significantly increased spatial DoFs (or transmission modes) [14], [15]. Owing to the increased spatial DoFs, it is expected that the spectrum efficiency can be naturally enhanced in the near-field region.

Unfortunately, the widely considered hybrid precoding architecture for XL-MIMO can hardly benefit from the increased DoFs provided by the near-field LoS path. In the far-field MIMO channel, due to the limited DoFs, the reduced number of RF chains for the classical hybrid precoding is still larger than the spatial DoFs. Thus, the classical hybrid precoding with a much reduced number of RF chains can fully utilize the spatial DoFs to achieve the near-optimal spectrum efficiency in the far-field region [16]. By contrast, this reduced number of RF chains is much smaller than the increased DoFs in the near-field region, resulting in a very limited number of data streams. That is to say, the classical hybrid precoding architecture designed for far-field communications can hardly utilize the increased spatial DoFs in the near-field region. To the best of our knowledge, this important problem of how to exploit the extra spatial DoFs brought by the near-field effect to improve the capacity has not been studied in the literature.

B. Our Contributions

To fill in this gap, in this paper, the theoretical capacity of the near-field channel is analyzed, and the precoding architecture for near-field MIMO communications is proposed¹. The main contributions of this paper can be summarized as follows:

- We introduce the eigenproblem in the electromagnetic theory to investigate the communication capacity of the near-field LoS channel. First, the increased DoFs are estimated based on the eigenproblem of prolate spheroidal wave functions. The effectiveness of the approximation of the singular values of the near-field LoS channel is verified by numerical simulations. Then, the channel capacity of the near-field LoS channel is analyzed, which reveals the channel capacity improvement in the near-field region.
- We propose a distance-aware precoding (DAP) architecture, which provides a new possibility to improve the capacity by utilizing the distance-related DoFs in the near-field region. The key idea is to adaptively adjust the number of RF chains to match the DoFs in the near-field region. Compared with the classical hybrid precoding architecture where the number of RF chains is fixed and limited, extra RF chains are equipped in the proposed DAP architecture, where each RF chain can

be flexibly configured to active or inactive. To realize this structure, a dedicated selection circuit is inserted to connect phase shifters to activated RF chains, which controls the selection pattern between the RF chains and array elements.

- Based on the DAP architecture, a DAP algorithm is proposed to improve the spectrum efficiency. In the proposed DAP algorithm, the number of activated RF chains is adaptively optimized according to the DoFs of the channel. Since the eigenvalues are close to each other in the near-field region, a near-field subarray partitioning algorithm is performed to optimize the selection matrix which represents the linking pattern between the RF chains and phase shifters to get a balanced subarray structure. Then, the corresponding digital precoder and analog precoder can be obtained utilizing the sub-connected feature. Finally, simulation results verify that, the proposed DAP scheme can efficiently utilize the extra DoFs to improve the spectrum efficiency and energy efficiency in the near-field region.

C. Organization and Notation

The remainder of the paper is organized as follows. Section II introduces the XL-MIMO communication system model in the near-field region, and compares the relationship between the near-field LoS channel and far-field LoS channel. Section III theoretically investigates the DoFs of the near-field LoS channel and provides an approximation method for the channel capacity. In Section IV, the DAP architecture is proposed. In Section V, the DAP algorithm is illustrated in detail. Simulation results are provided in Section VI, and conclusions are drawn in Section VII.

Notations: \mathbb{C} denotes the set of complex numbers; $[\cdot]^{-1}$, $[\cdot]^T$, $[\cdot]^H$ and $\text{diag}(\cdot)$ denote the inverse, transpose, conjugate-transpose and diagonal operations, respectively; $\|\cdot\|_F$ denotes the Frobenius norm of the matrix; $\angle[\cdot]$ denotes the angle of its complex argument; \mathbf{I}_N is an $N \times N$ identity matrix; $[a]^+$ represents $\max\{0, a\}$; finally $\mathbf{1}_L$ indicates an L -length vector with all elements being 1.

II. SYSTEM MODEL

In this paper, we consider a single-user XL-MIMO communication system. The transmitter and receiver are equipped with N_t and N_r antennas, respectively. To enable the transmission of N_s data streams, the transmitter and receiver contain N_t^{RF} and N_r^{RF} RF chains, satisfying $N_s \leq N_t^{\text{RF}} \leq N_t$ and $N_s \leq N_r^{\text{RF}} \leq N_r$. We assume that the number of RF chains equals the number of data streams for both transmitter and receiver. Thus, the $N_s \times 1$ symbol vector \mathbf{s} is followed by a $N_s \times N_s$ digital precoder \mathbf{F}_D and $N_t \times N_s$ analog precoder \mathbf{F}_A . The received signal is expressed as

$$\mathbf{y} = \mathbf{H}\mathbf{F}_A\mathbf{F}_D\mathbf{s} + \mathbf{n}, \quad (1)$$

where \mathbf{y} denotes the $N_r \times 1$ received vector, \mathbf{H} is the $N_r \times N_t$ channel matrix, and \mathbf{n} represents the noise vector $\mathbf{n} = [n_1, n_2, \dots, n_{N_r}]$, whose entities are mutually independent and follow the complex Gaussian distribution $\mathcal{CN}(0, \sigma_n^2)$.

¹Simulation codes are provided to reproduce the results presented in this paper: <http://oa.ee.tsinghua.edu.cn/dailinglong/publications/publications.html>.

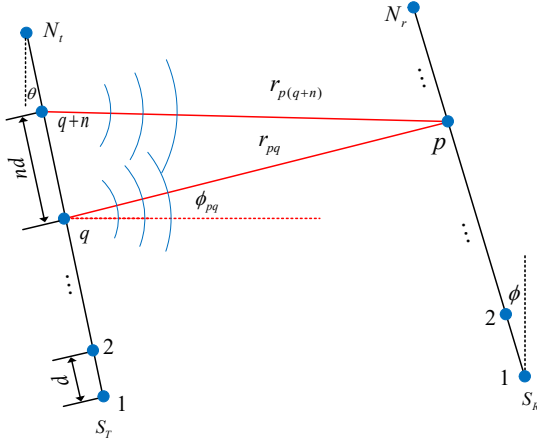


Fig. 1. The near-field geometric channel model of two non-parallel arrays.

Due to the high attenuation of millimeter-wave and terahertz bands, LoS path plays a dominant role in the XL-MIMO channel. Therefore, the classical far-field channel can be approximated by [3]

$$\mathbf{H} = \sum_{l=1}^L \alpha_l \Lambda_r(\phi_l^r) \Lambda_t(\phi_l^t) \mathbf{a}_r(\phi_l^r) \mathbf{a}_t^H(\phi_l^t) \quad (2)$$

$$\approx \alpha_{\text{LoS}} \Lambda_r(\phi_{\text{LoS}}^r) \Lambda_t(\phi_{\text{LoS}}^t) \mathbf{a}_r(\phi_{\text{LoS}}^r) \mathbf{a}_t^H(\phi_{\text{LoS}}^t),$$

where α_{LoS} (α_l) is the gain of the LoS (l^{th}) path, ϕ_{LoS}^t (ϕ_l^t) and ϕ_{LoS}^r (ϕ_l^r) are the azimuth angles of departure and arrival (AoDs/AoAs) for the LoS (l^{th}) path, respectively. The functions $\Lambda_t(\phi_{\text{LoS}}^t)$ and $\Lambda_r(\phi_{\text{LoS}}^r)$ represent the antenna element gain for the transmitter and receiver at the corresponding angle, respectively. The antenna array response vectors \mathbf{a}_t and \mathbf{a}_r are introduced to capture the spatial correlation characteristics for MIMO communications. For an N -element uniform linear array (ULA), the far-field array response vector $\mathbf{a}(\phi)$ can be written as

$$\mathbf{a}(\phi) = \frac{1}{\sqrt{N}} [1, e^{j\frac{2\pi}{\lambda} d \sin \phi}, \dots, e^{j(N-1)\frac{2\pi}{\lambda} d \sin \phi}]^T, \quad (3)$$

where d denotes the element spacing, and λ denotes the carrier wavelength. Note that the far-field channel in (2) has a low rank, i.e., it has very limited DoFs. Therefore, with much fewer RF chains than the number of antennas, the classical hybrid precoding architecture can fully utilize the limited spatial DoFs to achieve the near-optimal spectrum efficiency.

However, with the extremely large number of antennas in both the transmitter and receiver in XL-MIMO, receivers may lie in the near-field region of the transmitter. Then, the far-field LoS channel based on planar wave assumptions in (2) is no longer accurate to describe the LoS channel in the near-field region, where the channel has to be modeled by spherical wave assumptions. As shown in Fig. 1, based on the geometric free space assumption [4], the near-field LoS channel can be modeled as

$$\mathbf{H} = \begin{bmatrix} \alpha_{11} e^{-j\frac{2\pi}{\lambda} r_{11}} & \dots & \alpha_{1N_t} e^{-j\frac{2\pi}{\lambda} r_{1N_t}} \\ \vdots & \ddots & \vdots \\ \alpha_{N_r 1} e^{-j\frac{2\pi}{\lambda} r_{N_r 1}} & \dots & \alpha_{N_r N_t} e^{-j\frac{2\pi}{\lambda} r_{N_r N_t}} \end{bmatrix}, \quad (4)$$

where r_{pq} and α_{pq} denote the distance and normalized path gain between p^{th} receiver antenna and q^{th} transmitter antenna, respectively.

It is worth noting that ULA is considered in this paper for simplicity, and it is straightforward to deploy the more realistic planar arrays and the main results remain the same².

Proposition 1: The far-field channel model in (2) is a particular case of the near-field channel in (4) when the array apertures $(N_r - 1)d$ and $(N_t - 1)d$ can be negligible compared with the communication distance r .

Proof: The proof is provided in Appendix A. ■

Moreover, it can be obtained that the rank of the far-field LoS channel in (2) is only 1. As a contrast, the rank of the near-field LoS channel in (4) can be huge, or the channel can even be full rank, which indicates a significantly increased multiplexing gain compared with the far-field LoS channel. To investigate the capacity gain in the near-field region, the available DoFs need to be approximated.

III. DOFS AND CAPACITY ANALYSIS IN NEAR-FIELD

In this section, the theoretical analysis of DoFs and channel capacity in the near-field region is provided. In Section III-A, we analyze the increased available DoFs by introducing eigenproblems in the electromagnetic wave theory. In Section III-B, to avoid the complicated process of channel decomposition, an estimation of the channel capacity in the near-field region is provided. Finally, we investigate the capacity curve in the near-field region in Section III-C.

A. DoFs Estimation of the Near-field LoS Channel

It is difficult to directly analyze the DoFs, to be precise, the singular values, of the near-field LoS channel. It has been proved that, through the Nyquist space sampling theorem, the half-wavelength spaced antennas can be equivalently modeled as continuous apertures without loss of accuracy. Therefore, we could generalize the classical discrete antenna arrays to continuous apertures. By incorporating the analysis method in electromagnetic field theory, we are able to estimate the DoFs in the near-field region.

In [14], the DoFs of a pair of *parallel* positioned continuous linear arrays are researched. However, the assumption of parallel arrays is hard to be guaranteed in real communication systems. Therefore, the DoFs of *non-parallel* linear arrays are needed to be analyzed. In this paper, we consider a pair of *non-parallel* positioned continuous linear arrays³ as in Fig. 1. The angle between the array and vertical line is denoted by θ and ϕ for transmitter and receiver, respectively. The centers of the two arrays are positioned on the same level, with separation distance denoted by r . We consider a location vector denoted by \mathbf{r} . The area within the transmitter and receiver is denoted by S_T and S_R , respectively. Since the arrays are modeled

²We also assume that the number of antennas for both the transmitter and receiver is large. This scenario can happen in backhuls or internet of vehicles in future 6G.

³We assume that the arrays are modeled in 3D space, where the linear array is along with the y-direction with the angle of θ or ϕ . The width of the array in other directions is small and can be neglected. Therefore, the current on the antenna array is not restricted along with the array.

as continuous apertures, we can assume the monochromatic source $\psi(\mathbf{r}_T)$ on the transmitter Tx that generate waves $\phi(\mathbf{r}_R)$ on the receiver array Rx, which derives from Green's function as

$$\phi(\mathbf{r}) = \int_{S_T} G(\mathbf{r}, \mathbf{r}_T) \psi(\mathbf{r}_T) d\mathbf{r}_T, \quad (5)$$

where $G(\mathbf{r}, \mathbf{r}_T)$ denotes the corresponding Green's function. Based on the spherical wave assumptions in the near-field region, the possible waves resulting from a single point source \mathbf{r}_1 in free space can be modeled as

$$G(\mathbf{r}, \mathbf{r}_1) = \frac{\exp(-jk|\mathbf{r} - \mathbf{r}_1|)}{4\pi|\mathbf{r} - \mathbf{r}_1|}, \quad (6)$$

where the negative sign inside the exponential represents the outgoing directions. Similar to singular value decomposition (SVD), we introduce the function as

$$K(\mathbf{r}'_T, \mathbf{r}_T) = \int_{S_R} G^*(\mathbf{r}_R, \mathbf{r}'_T) G(\mathbf{r}_R, \mathbf{r}_T) d\mathbf{r}_R. \quad (7)$$

Therefore, following the formulation in [14], we could derive a series of eigenproblems as

$$v\psi(\mathbf{r}_T) = \int_{S_T} K(\mathbf{r}'_T, \mathbf{r}_T) \psi(\mathbf{r}'_T) d\mathbf{r}'_T, \quad (8)$$

where v denotes the eigenvalue corresponding to the function $\psi(\cdot)$.

Proposition 2: The solution to the eigenproblem in (8) could be further simplified as

$$v_n \psi_n(c_y, \xi_T) = \int_{-1}^1 \frac{\sin[c_y(\xi_T - \xi'_T)]}{\pi(\xi_T - \xi'_T)} \psi_n(c_y, \xi'_T) d\xi'_T, \quad (9)$$

where $\psi_n(c_y, \xi_T)$ represents a series of complete orthonormal basis sets, in which ξ_T and ξ'_T represent the scaled length with given $\xi_T = \eta_T / ((N_t - 1)d \cos \theta)$. The dimensionless parameter c_y represents the equivalent bandwidth along the array aperture defined as

$$c_y = \frac{\pi(N_t - 1)(N_r - 1)d^2 \cos \theta \cos \phi}{2\lambda r}. \quad (10)$$

Proof: The proof is provided in Appendix B. ■

Based on the equation in (9), it can be proved that the prolate spheroidal wave functions (PSWFs) are the solutions to the eigenproblem [17]. The normalized distinct eigenvalues follow the inequation as

$$1 \geq v_0 > v_1 > v_2 > \dots > 0. \quad (11)$$

In the electromagnetic field theory, the eigenvalues represent the coupling coefficients between orthogonal basis functions, which are equivalent to the square of singular values through SVD in communications. Therefore, the singular values of the near-field LoS channel can be approximated with the eigenvalues of PSWFs. If we consider a pair of parallel arrays, the eigenvalues of PSWFs are consistent with the singular values derived from SVD for a pair of parallel ULA as in Fig. 2. It indicates that the DoFs can be estimated without complicated SVD when the size of channel matrix \mathbf{H} becomes huge as the number of antennas scales up. It is worth noting that, in the beginning, the eigenvalues fall off slowly. However,

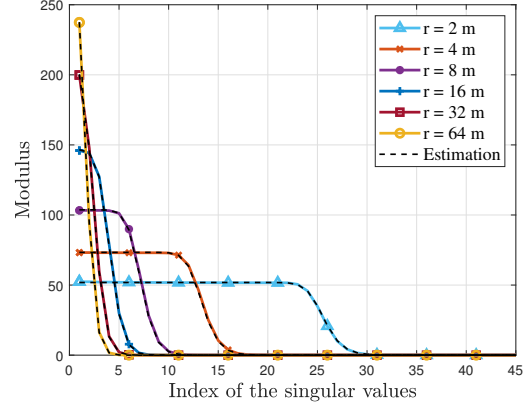


Fig. 2. Calculated and estimated singular values for a pair of parallel 256 ULA antennas. Colored solid lines represent the calculated singular values based on SVD on different distances, while black dashed lines are derived with eigenvalues of PSWFs of equal channel power for corresponding distance.

there is a critical value after which the eigenvalues of PSWFs (or singular values of the channel) fall off exponentially, which can also be derived with the PSWFs as

$$N_{\text{DoF}}(r) \approx \frac{2}{\pi} c_y = \frac{(N_t - 1)(N_r - 1)d^2 \cos \theta \cos \phi}{\lambda r}. \quad (12)$$

As illustrated in (12), as the transmitter-receiver distance decreases, the critical value increases, which enables the communication systems to transmit multiple data streams. For special parallel cases, when setting $\theta = 0$ and $\phi = 0$, the estimated DoFs can be simplified as

$$N_{\text{DoF}}(r) \approx \frac{(N_t - 1)(N_r - 1)d^2}{\lambda r}, \quad (13)$$

which is consistent with the results in [14]. Note that $(N_t - 1)d \cos \theta$ represents the effective length of the transmitter array projected along the y-axis. Therefore, a pair of non-parallel arrays is equivalent to the parallel arrays with the effective length projected perpendicularly to the line of array centers for DoFs estimation.

It has been theoretically proved that, unlike classical far-field LoS channel, the spatial DoFs significantly scales up as the distance decreases in the near-field LoS channel. It is expected that channel capacity can be enhanced by utilizing the increasing DoFs for spatial multiplexing in near-field communications.

B. Channel Capacity Analysis

As mentioned above, the near-field channel differs from the far-field channel in that the DoFs significantly increase within the LoS path. The channel capacity can also benefit from the increased DoFs. If we consider a MIMO system model as in (1), the channel capacity can be formulated as

$$\begin{aligned} C &= \max_{\mathbf{F}} \log_2 \left| \mathbf{I} + \frac{1}{\sigma_n^2} \mathbf{H} \mathbf{F} \mathbf{F}^H \mathbf{H}^H \right| \\ &= \sum_{i=1}^{\min(N_t, N_r)} \log_2 \left(1 + \frac{p_i}{\sigma_n^2} \lambda_i^2 \right), \end{aligned} \quad (14)$$

where λ_i denotes the i^{th} singular value of channel matrix, p_i denotes the power allocated to i^{th} sub-channel according to

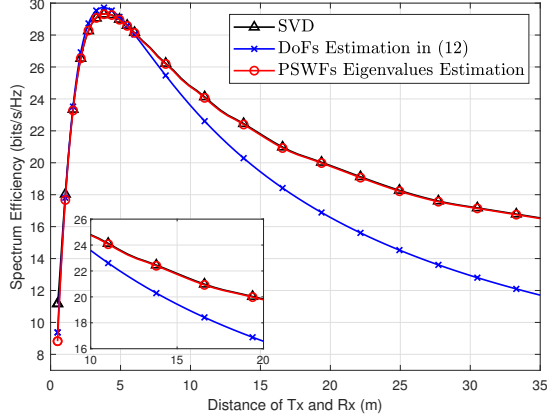


Fig. 3. Calculated and estimated channel capacity in the near-field region. Orange line represents the calculated channel capacity, which the purple and red lines denote the estimated channel capacity with DoFs and eigenvalues of PSWFs respectively. The total transmitted SNR is set to be 15 dB.

the classical water-filling method [18]. \mathbf{F} denotes the fully-digital precoding matrix with the power constraints.

To find more insights, we consider a case where the array apertures are parallel positioned. Through perfect transmission power control, we could assume the large-scale fading can be ignored, thus the Frobenius norm of the channel matrix share the same value over different distances r . According to the estimated singular values of PSWFs in (9), the capacity of the near-field LoS channel can be rewritten as

$$\begin{aligned}
 C &\stackrel{(a)}{\approx} \sum_{i=1}^{N_{\text{DoF}}} \log_2 \left(1 + \frac{p_i}{\sigma_n^2} \lambda_i^2 \right) \\
 &\stackrel{(b)}{\approx} N_{\text{DoF}} \log_2 \left(1 + \frac{P_{\text{tot}} P_{\text{H}}}{\sigma_n^2 N_{\text{DoF}}^2} \right) \\
 &\approx \frac{(N_t - 1)(N_r - 1)d^2}{\lambda r} \\
 &\quad \times \log_2 \left(1 + \frac{P_{\text{tot}} P_{\text{H}} \lambda^2 r^2}{\sigma_n^2 (N_t - 1)^2 (N_r - 1)^2 d^4} \right),
 \end{aligned} \tag{15}$$

where N_{DoF} denotes the DoFs in the near-field LoS channel as in (12), P_{H} denotes the power of the channel. Approximation (a) is obtained by assuming that the first N_{DoF} sub-channels take up the main power of all the sub-channels. Approximation (b) is obtained by assuming the singular values fall off slowly within the dominant N_{DoF} sub-channels and thus equal power is allocated to each sub-channel. According to Fig. 2, the assumptions above are reasonable for a pair of parallel ULA. Here we have three ways to obtain the channel capacity in the near-field region, by precisely SVD and water-filling method, by assuming an equal power allocation as in (15) and by water-filling method using eigenvalues of PSWFs. The simulation results are illustrated in Fig. 3.

It is shown from Fig. 3 that, the capacity significantly increases as the transmission distance decreases. Compared with the classical estimation of DoFs as in [14], the estimation with PSWFs eigenvalues approximates better to the channel capacity for large transmission distance r . It reveals a theoretical method to fastly estimate the channel capacity in the near-field region without calculation-consuming SVD process. Although the simulation is carried out under the strict

assumptions that the arrays have to be parallel positioned, the method can also be generalized to non-parallel arrays which removes the degeneracy of eigenvalues as illustrated in [19]. The capacity analysis of non-parallel linear arrays in the near-field region is also one direction for future research.

C. Discussions on Channel Capacity

Based on the approximation results in Fig. 3, it is worth noting that channel capacity does not monotonically decrease as the distance scales up. We explain it with the approximation result in equation (15). The denominator within the logarithm contains square of DoFs while the logarithm is also multiplied by DoFs. By derivation, the capacity is maximized when DoFs achieve N_{DoF}^* which satisfies

$$\left(\frac{N_{\text{DoF}}^{*2} \sigma_n^2}{P_{\text{tot}} P_{\text{H}}} + 1 \right) \log_2 \left(1 + \frac{P_{\text{tot}} P_{\text{H}}}{N_{\text{DoF}}^{*2} \sigma_n^2} \right) = \frac{2}{\ln 2}. \tag{16}$$

Through numerical calculations, the solution to the transcendental equation in (16) can be obtained by $N_{\text{DoF}}^* \approx \sqrt{0.255 \frac{P_{\text{tot}} P_{\text{H}}}{\sigma_n^2}}$. The transmitter-receiver distance r can also be estimated with N_{DoF}^* . The special phenomenon originates from the spread of the channel power. For near-field communications, although the DoFs scale up as the distance decreases, the energy of the channel is also averagely allocated to more orthogonal sub-channels, reducing the equivalent signal-noise ratio (SNR) within each sub-channel. Therefore, the capacity for each sub-channel decreases as the DoFs increase, resulting in non-monotonic increasing capacity as distance decreases⁴.

From Fig. 2 and Fig. 3, as the communication distance decreases, the capacity of near-field LoS channel dramatically (but not monotonically) increases. Therefore, it is expected to utilize the increase DoFs to improve the spectrum efficiency in the near-field region.

IV. PROPOSED DAP ARCHITECTURE

With the small DoFs of the far-field LoS channel, the classical far-field hybrid precoding with a reduced number of RF chains could achieve the near-optimal spectrum efficiency. However, with the increased DoFs of the near-field LoS channel, classical hybrid precoding with limited RF chains is unable to approach the optimal spectrum efficiency. According to our best knowledge, an architecture that can flexibly change the number of RF chains to match the increased DoFs in the near-field region is still a blank.

To efficiently utilize the DoFs of the near-field LoS channel, fully-digital precoding is able to achieve the optimal spectrum efficiency regardless of in the far-field region or near-field region. Nevertheless, fully-digital precoding requires the number of RF chains equal to the number of transmitter antennas, which leads to the unaffordable power consumption in millimeter-wave and terahertz bands. It is worth noting that the mobile receiver may sometimes be located in the far-field region and be located in the near-field region at

⁴It is worth noting that, here we assume the large-scale fading is not considered in our model. When large-scale fading is incorporated, the capacity will be monotone increasing as the distance decreases.

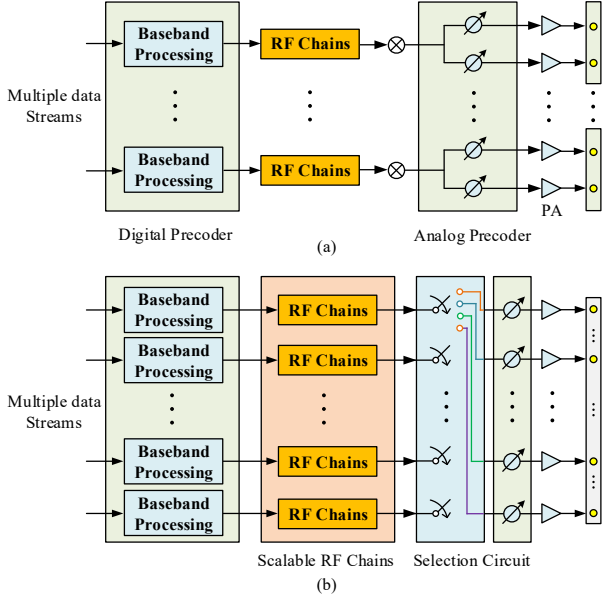


Fig. 4. Comparison of the precoding architecture: (a) Classical sub-connected hybrid precoding architecture; (b) Proposed DAP architecture.

other times, resulting in varying distance-related DoFs of the MIMO channel as illustrated in (12). Actually, the extra activated RF chains more than the DoFs of the channel can be turned off without significant loss of spectrum efficiency. Motivated by this observation, we propose a DAP architecture that can flexibly control the number of activated RF chains to match the varying DoFs, which can significantly increase the spectrum efficiency in the near-field region. The proposed DAP architecture is shown in Fig. 4.

Specifically, the sub-connected architecture is adopted in the proposed DAP architecture to save unnecessary power consumptions as in [20]. In the DAP architecture, each antenna element only connects to one RF chain. To enable a variable number of RF chains, extra RF chains are equipped in the transmitter and receiver and each RF chain can be configured to active or inactive. In addition, each antenna element can dynamically select one arbitrary RF chain through a selection circuit. The RF chains without any connection can be regarded as inactive, thus enabling the control of the number of RF chains.

The advantage of introducing the selection circuit is two-fold. First, the selection pattern between RF chains and antennas enables the choice of the active RF chain numbers, which can be adaptively adjusted according to the available channel DoFs. Second, the selection pattern also provides a new dimension to design the precoding, which can further enhance the spectrum efficiency.

Based on the proposed DAP structure, the received signal in equation (1) can be rewritten as

$$\mathbf{y} = \mathbf{H}\mathbf{F}_A\mathbf{F}_S\mathbf{F}_D\mathbf{s} + \mathbf{n}, \quad (17)$$

where the $N_t \times N_s$ selection matrix \mathbf{F}_S represents the adjustable selection matrix between array elements and activated RF chains. Each entity of \mathbf{F}_S is assigned either 0 or 1. Since each antenna element can only select one RF chain, each row of \mathbf{F}_S contains one element that equals 1. Besides, since

the analog precoder is implemented by analog phase shifters, \mathbf{F}_A has an extra constant norm constraint. Different from the classical hybrid precoding architecture, the introduction of selection matrix changes the size of analog precoder, which is a $N_t \times N_t$ diagonal matrix with constant norm. The feasible set of the analog precoder can be written as

$$\mathcal{F} \triangleq \left\{ \text{diag}(\tilde{\theta}_1, \dots, \tilde{\theta}_{N_t}) \mid \tilde{\theta}_i \in \mathbb{C}, |\tilde{\theta}_i| = 1, \forall i \right\}. \quad (18)$$

Remark 1: Unlike the classical hybrid precoding architecture where the number of data streams N_s is fixed, the proposed DAP architecture could flexibly adjust the number of data streams N_s . Therefore, the optimization of the number of RF chains N_s should also be taken into account.

When considering the precoding algorithm to maximize the spectrum efficiency, we can assume that an optimal combiner is employed at the receiver side [3]. Thus, the spectrum efficiency can be written as

$$R = \log_2 \left(\left(\mathbf{I} + \frac{1}{\sigma_n^2} \mathbf{H}\mathbf{F}_A\mathbf{F}_S\mathbf{F}_D\mathbf{F}_D^H\mathbf{F}_S^H\mathbf{F}_A^H\mathbf{H}^H \right) \right). \quad (19)$$

Unlike the previous work which assumes an equal power allocation over different sub-channels [20], we consider a power allocation process according to the classical water-filling method, which will be detailed described in the following section.

V. PROPOSED DAP ALGORITHM

In this section, we propose a DAP algorithm for the proposed DAP structure to improve the spectrum efficiency for near-field XL-MIMO communications. In Section V-A, we provide an overview of the DAP algorithm. The design of digital precoder, selection matrix, and analog precoder are introduced from Section V-B to Section V-E.

A. Overview of the DAP Algorithm

Based on the proposed DAP structure, the key problem is to determine the number of data streams N_s . As N_s increases, the proposed DAP architecture approaches the fully-digital precoding architecture, which is considered to be ideal in terms of spectrum efficiency with high power consumption. According to the analysis in Section III, the DoFs can be well estimated in the near-field region. Similar to the hybrid precoding scheme in the far-field region, a reduced number of RF chains can be deployed to match the DoFs in the near-field region to reduce power consumption as well as achieve the near-optimal spectrum efficiency. With fixed data streams N_s , the optimization can be formulated as

$$\begin{aligned} \mathcal{P} : & \max_{\mathbf{F}_A, \mathbf{F}_S, \mathbf{F}_D} R(\mathbf{F}_A, \mathbf{F}_S, \mathbf{F}_D) \\ \text{s.t.} & C_1 : \|\mathbf{F}_A\mathbf{F}_S\mathbf{F}_D\|_F^2 \leq P_{\text{tot}} \\ & C_2 : \mathbf{F}_A \in \mathcal{F} \\ & C_3 : (\mathbf{F}_S)_{ij} \in \{0, 1\}, \forall i, j \\ & C_4 : \text{diag}(\mathbf{F}_S\mathbf{F}_S^H) = \mathbf{1}_{N_t}, \end{aligned} \quad (20)$$

where \mathcal{F} is the feasible set for analog precoder in (18). The precoding algorithm can be summarized into three stages.

Algorithm 1 Proposed DAP Algorithm.

Input: Channel \mathbf{H} , r , N_t and N_r .

Output: Optimized data streams N_s^{opt} , digital precoder $\mathbf{F}_D^{\text{opt}}$, analog precoder $\mathbf{F}_A^{\text{opt}}$ and selection matrix $\mathbf{F}_S^{\text{opt}}$

- 1: Obtain the eigenvalues of PSWFs in (9) with distance r ;
 - 2: Set the data streams N_s^{opt} by N_{DoF} calculated by water-filling method with eigenvalues of PSWFs;
 - 3: Obtain subarray sets $\mathcal{S}_1, \mathcal{S}_2, \dots, \mathcal{S}_{N_s^{\text{opt}}}$ by **Algorithm 2**;
 - 4: Calculate $\mathbf{F}_S^{\text{opt}}$ according to (26)
 - 5: Obtain $\mathbf{F}_A^{\text{opt}}$ by (35);
 - 6: Obtain $\mathbf{F}_D^{\text{opt}}$ by (22);
 - 7: **return** N_s^{opt} , $\mathbf{F}_A^{\text{opt}}$, $\mathbf{F}_S^{\text{opt}}$, $\mathbf{F}_D^{\text{opt}}$.
-

First, the number of data streams as well as the number of activated RF chains N_s is determined according to the DoFs for the near-field LoS channel. Second, we determine the selection matrix \mathbf{F}_S by optimizing the partitioning pattern of the arrays, which aims to choose the best pattern of subarrays that maximizes the spectrum efficiency. Third, we can obtain the corresponding analog precoder \mathbf{F}_A and digital precoder \mathbf{F}_D that satisfy the constraints in C_1 and C_2 . The proposed DAP algorithm can be summarized in **Algorithm 1**.

B. Estimation of Available Data Streams N_s

The analysis of channel DoFs is provided in Section III-A. In (12) and (13), the DoFs can be estimated well for small distance r . However, the eigenvalues of PSWFs offer a better approximation of the singular values of the near-field LoS channel. Therefore, we adopt a water-filling process utilizing the eigenvalues of PSWFs to obtain the DoFs. Precisely, N_{DoF} is equal to the number of non-zero power allocated to the sub-channels in the water-filling process. After obtaining N_{DoF} , similar to the classical hybrid precoding architectures, we set $N_s = N_{\text{DoF}}$ to fully utilize the spatial multiplexing gain for capacity improvement in the near-field region at minimum energy consumption.

Remark 2: The choice of $N_s = N_{\text{DoF}}$ is not the optimal choice, since the increased number of RF chains could further approach to the fully-digital precoding scheme. Yet it is an essential condition that $N_s \geq N_{\text{DoF}}$ to utilize the spatial multiplexing gain. In the following sections, we will compare the performance with the different number of data streams to reveal the rationality of the choice of N_s .

C. Optimization of Digital Precoder \mathbf{F}_D

With fixed number of data streams N_s , to simplify the formulation in (20), we define the effective channel $\mathbf{H}_e \triangleq \mathbf{H}\mathbf{F}_A\mathbf{F}_S$. The optimization object can be rewritten as

$$R = \log_2 \left(\left| \mathbf{I} + \frac{1}{\sigma_n^2} \mathbf{H}_e \mathbf{F}_D \mathbf{F}_D^H \mathbf{H}_e^H \right| \right). \quad (21)$$

By assuming the SVD of effective channel $\mathbf{H}_e = \mathbf{U}_e \mathbf{\Sigma}_e \mathbf{V}_e^H$, we can obtain the solution of digital precoder

$$\mathbf{F}_D^{\text{opt}} = \mathbf{V}_e \mathbf{\Gamma}, \quad (22)$$

where $\mathbf{\Gamma}$ denotes a diagonal power allocation matrix $\mathbf{\Gamma} = \text{diag}(\sqrt{p_1}, \sqrt{p_2}, \dots, \sqrt{p_{N_s}})$. Then the spectrum efficiency can be rewritten as

$$R = \sum_{i=1}^{N_s} \log_2 \left(1 + \frac{\lambda_i^2(\mathbf{H}\mathbf{F}_A\mathbf{F}_S)p_i}{\sigma_n^2} \right), \quad (23)$$

where $\lambda_i^2(\cdot)$ denotes the i^{th} singular value of the argument matrix. And the elements of $\mathbf{\Gamma}$ can be calculated through the water-filling process in which

$$p_i = \left(\frac{1}{\mu} - \frac{\sigma_n^2}{\lambda_i^2(\mathbf{H}\mathbf{F}_A\mathbf{F}_S)} \right)^+. \quad (24)$$

The auxiliary variable μ is determined by the power constraint that $\sum_i p_i = P_{\text{tot}}$. Therefore, the digital precoder \mathbf{F}_D can be easily obtained when analog precoder \mathbf{F}_A and selection matrix \mathbf{F}_S are fixed.

D. Optimization of Selection Matrix \mathbf{F}_S

The selection matrix \mathbf{F}_S represents the linking pattern of the RF chains and array elements. Here we denote the set of array indices that connect to the i^{th} RF chain as

$$\mathcal{S}_i = \{n_{i1}, n_{i2}, \dots, n_{i|\mathcal{S}_i|}\}, \quad (25)$$

where $|\mathcal{S}_i|$ denotes the number of entities in \mathcal{S}_i . The selection matrix can be directly derived from \mathcal{S}_i as

$$[\mathbf{F}_S]_{j,i} = \begin{cases} 1, & j \in \mathcal{S}_i, \\ 0, & j \notin \mathcal{S}_i. \end{cases} \quad (26)$$

To get the optimal partitioning of subarrays, according to Jensen's inequality, the formulation of spectrum efficiency can be further rewritten as

$$\begin{aligned} R &= \sum_{i=1}^{N_s} \log_2 \left(1 + \frac{\lambda_i^2(\mathbf{H}\mathbf{F}_A\mathbf{F}_S)p_i}{\sigma_n^2} \right) \\ &\leq N_s \log_2 \left(1 + \frac{1}{N_s} \sum_{i=1}^{N_s} \frac{\lambda_i^2(\mathbf{H}\mathbf{F}_A\mathbf{F}_S)p_i}{\sigma_n^2} \right). \end{aligned} \quad (27)$$

As illustrated in Section III-A, the singular values of the near-field LoS channel are close to each other if N_s satisfies $N_s \leq N_{\text{DoF}}$, which is consistent with our settings. Thus the approximation is tight for near-field XL-MIMO communication systems. Then, the optimization of selection matrix \mathbf{F}_S and analog precoder \mathbf{F}_A can be simplified as

$$(\mathbf{F}_A^{\text{opt}}, \mathbf{F}_S^{\text{opt}}) = \underset{\mathbf{F}_A, \mathbf{F}_S}{\text{argmax}} \sum_{i=1}^{N_s} \lambda_i^2(\mathbf{H}\mathbf{F}_A\mathbf{F}_S). \quad (28)$$

Utilizing the feature of \mathbf{F}_S that all elements in each row of \mathbf{F}_S are equal 0 except one element, \mathbf{F}_S can be reformulated as

$$\mathbf{F}_S = \mathbf{P}_S \tilde{\mathbf{F}}_S, \quad (29)$$

where \mathbf{P}_S is a permutation matrix and $\tilde{\mathbf{F}}_S$ follows a block diagonal pattern of

$$\tilde{\mathbf{F}}_S = \begin{bmatrix} \mathbf{1}_{\mathcal{S}_1} & 0 & \cdots & 0 \\ 0 & \mathbf{1}_{\mathcal{S}_2} & \cdots & 0 \\ \vdots & \vdots & \ddots & \vdots \\ 0 & 0 & \cdots & \mathbf{1}_{\mathcal{S}_{N_s}} \end{bmatrix}, \quad (30)$$

where $\mathbf{1}_{\mathcal{S}_i}$ denotes a vector with $|\mathcal{S}_i|$ elements that are equal to 1. Due to the property of permutation matrix, we can switch the order of the diagonal analog precoder \mathbf{F}_A and permutation matrix \mathbf{P}_S as

$$\mathbf{H}\mathbf{F}_A\mathbf{P}_S\tilde{\mathbf{F}}_S = \mathbf{H}\mathbf{P}_S\tilde{\mathbf{F}}_A\tilde{\mathbf{F}}_S, \quad (31)$$

where $\tilde{\mathbf{F}}_A$ denotes the diagonal analog precoder with a permutation operation. A brief proof is provided in Appendix C.

Due to the block diagonal feature of $\tilde{\mathbf{F}}_S$, $\tilde{\mathbf{H}} = \mathbf{H}\mathbf{P}_S$ can be classified by columns as submatrices $\tilde{\mathbf{H}} = [\mathbf{H}_{S_1}, \dots, \mathbf{H}_{S_{N_s}}]$. Therefore, the optimization object in (28) can be rewritten as

$$\begin{aligned} & \max_{\mathbf{F}_A, \mathbf{F}_S} \sum_{i=1}^{N_s} \lambda_i^2(\mathbf{H}\mathbf{F}_A\mathbf{F}_S) \\ &= \max_{\mathbf{F}_A, \mathbf{F}_S} \sum_{i=1}^{N_s} \lambda_i^2(\mathbf{H}\mathbf{P}_S\tilde{\mathbf{F}}_A\tilde{\mathbf{F}}_S) \\ &= \max_{\mathbf{F}_A, \mathbf{F}_S} \left\| \mathbf{H}\mathbf{P}_S\tilde{\mathbf{F}}_A\tilde{\mathbf{F}}_S \right\|_F^2 \\ &= \max_{\mathbf{F}_A, \mathbf{F}_S} \left\| [\mathbf{H}_{S_1}\mathbf{f}_1, \dots, \mathbf{H}_{S_{N_s}}\mathbf{f}_{N_s}] \right\|_F^2 \\ &\stackrel{(a)}{\approx} \sum_{i=1}^{N_s} \lambda_1(\mathbf{H}_{S_i}^H\mathbf{H}_{S_i}), \end{aligned} \quad (32)$$

where \mathbf{f}_i denotes non-zero elements of the i^{th} column of $\tilde{\mathbf{F}}_A\tilde{\mathbf{F}}_S$. The approximation (a) is derived by omitting the constant modulus constraints of \mathbf{F}_A . Therefore, the optimization object can be formulated as the summation of the largest singular value of submatrices. However, if we perform exhaustive searching to find all the sets \mathcal{S}_i that maximize the spectrum efficiency, the complexity will be unaffordable. Therefore, we propose a low-complexity algorithm to optimize the selection matrix \mathbf{F}_S by utilizing the normalized Minkowski ℓ_1 -norm.

It has been proved that Minkowski ℓ_1 -norm gives a good approximation of the largest singular value [21] as

$$\lambda_1(\mathbf{R}_S) \approx \hat{\lambda}_1(\mathbf{R}, S) = \frac{1}{|S|} \sum_{i \in S} \sum_{j \in S} |[\mathbf{R}]_{i,j}|. \quad (33)$$

Therefore, we could perform a low-complex greedy searching process to maximize the average Minkowski ℓ_1 -norm for each partitioning set \mathcal{S}_i . The proposed near-field subarray partitioning algorithm is summarized in **Algorithm 2**.

Different from other dynamic subarray design algorithms in [22]–[24], we aim to obtain subarrays with similar scales. As illustrated in Section III-A, the singular values of the near-field LoS channel are close to each other. Thus the scale of subarrays should be similar to generate equal beamforming gain. First, we initialize all the sets \mathcal{S} with uniformly distributed antennas. Then, we add the antennas to sets one by one. We select the j^{th} antenna with the largest absolute value of $|\mathbf{R}_{i,j}|$ in which j^{th} antenna is not added yet. If the cardinal of sets exceeds the maximum scale N_{bound} , we remove the m^{th} antenna with the least contribution and add it to the set with largest improvement. Finally, we check all the sets one by one to remove the least contributor, which aims to eliminate the influence of the manual initialization.

Algorithm 2 Near-Field Subarray Partitioning Algorithm.

Input: Channel \mathbf{H} , N_s , N_{bound} and N_t .

Output: $\mathcal{S}_1, \mathcal{S}_2, \dots, \mathcal{S}_{N_s}$

- 1: $\mathbf{R} = \mathbf{H}^H\mathbf{H}$, $\mathcal{S}_{\text{sel}} = \emptyset$, $n_{\text{group}} = \lfloor \frac{N_t}{N_s} \rfloor$
 - 2: Initialize $\mathcal{S}_i = \{i \cdot n_{\text{group}}\}$, $\mathcal{S}_{\text{sel}} \leftarrow \mathcal{S}_{\text{sel}} \cup \{i \cdot n_{\text{group}}\}$, for $i = 1, 2, \dots, N_s$
 - 3: **for** $k = 1 : N_t - N_s$ **do**
 - 4: $\{i_k, j_k\} = \underset{i \in \mathcal{S}_{\text{sel}}, j \notin \mathcal{S}_{\text{sel}}}{\text{argmax}} |[\mathbf{R}]_{i,j}|$
 - 5: $\hat{r} = \underset{r \in \{1, \dots, N_s\}}{\text{argmax}} \hat{\lambda}_1(\mathbf{R}, \mathcal{S}_r \cup \{j_k\}) - \hat{\lambda}_1(\mathbf{R}, \mathcal{S}_r)$
 - 6: $\mathcal{S}_{\text{sel}} \leftarrow \mathcal{S}_{\text{sel}} \cup j_k$, $\mathcal{S}_{\hat{r}} \leftarrow \mathcal{S}_{\hat{r}} \cup j_k$
 - 7: **if** $|\mathcal{S}_{\hat{r}}| \geq N_{\text{bound}}$ **then**
 - 8: $\hat{m} = \underset{m \in \mathcal{S}_{\hat{r}}}{\text{argmin}} |\mathbf{R}_{m,n}|$
 - 9: $\hat{r}' = \underset{r' \neq \hat{r}}{\text{argmax}} \hat{\lambda}_1(\mathbf{R}, \mathcal{S}_{r'} \cup \hat{m}) - \hat{\lambda}_1(\mathbf{R}, \mathcal{S}_{r'})$
 - 10: $\mathcal{S}_{\hat{r}} \leftarrow \mathcal{S}_{\hat{r}} \setminus \hat{m}$, $\mathcal{S}_{\hat{r}'} \leftarrow \mathcal{S}_{\hat{r}'} \cup \hat{m}$
 - 11: **end if**
 - 12: **end for**
 - 13: **for** $l = 1 : N_s$ **do**
 - 14: $\hat{m} = \underset{m \in \mathcal{S}_l}{\text{argmin}} |\mathbf{R}_{m,n}|$
 - 15: $\hat{r}' = \underset{r'}{\text{argmax}} \hat{\lambda}_1(\mathbf{R}, \mathcal{S}_{r'} \cup \hat{m}) - \hat{\lambda}_1(\mathbf{R}, \mathcal{S}_{r'})$
 - 16: $\mathcal{S}_{\hat{r}'} \leftarrow \mathcal{S}_{\hat{r}'} \setminus \hat{m}$, $\mathcal{S}_{\hat{r}'} \leftarrow \mathcal{S}_{\hat{r}'} \cup \hat{m}$
 - 17: **end for**
 - 18: **return** $\mathcal{S}_1, \mathcal{S}_2, \dots, \mathcal{S}_{N_s}$
-

Remark 3: It is worth noting that, as the number of data streams N_s increases, the heuristic dynamic subarray searching algorithm proposed in [22], [23] may result in a situation where some subarrays are totally empty. The degradation of subarrays causes inefficient usage of spatial DoFs in the near-field region, making the spectrum efficiency far less than optimal. Another greedy searching algorithm proposed in [24] aims to maximize the largest singular value of each submatrix one by one. In this way, the submatrices can hardly remain balanced to maximize the sum rate of all sub-channels. Therefore, the proposed partitioning algorithm is more suitable for near-field communication scenarios.

Since in each iteration, one antenna is added into one set, the convergence of the proposed algorithm is guaranteed. In the worst case where one set quickly achieves the maximum size, the complexity of the algorithm is estimated as $\mathcal{O}(N_t^2 + N_t N_{\text{bound}})$ as for comparing operations and $\mathcal{O}(N_s N_t N_{\text{bound}})$ as for add operations.

E. Optimization of Analog Precoder \mathbf{F}_A

As illustrated in (32), the optimal analog precoder corresponding to the i^{th} subarray can be formulated as

$$\angle(\mathbf{f}_{A,S_i}^{\text{opt}}) = \angle(\mathbf{v}_{S_i}), \quad (34)$$

where \mathbf{v}_{S_i} is the singular vector corresponding to the largest singular value of \mathbf{H}_{S_i} . Therefore, each array $\mathbf{f}_{A,S_i}^{\text{opt}}$ can be determined satisfying the constraints on the norm. Finally, the formulation of the analog precoder can be written as

$$\mathbf{F}_A^{\text{opt}} = \mathbf{P}_S \text{diag} \left(\left[(\mathbf{f}_{A,S_1}^{\text{opt}})^T, \dots, (\mathbf{f}_{A,S_{N_s}}^{\text{opt}})^T \right] \right) \mathbf{P}_S^T. \quad (35)$$

It is worth noting that, due to the constant norm constraints of \mathbf{F}_A , the close-form solution in (32) is an approximation of the optimal solution without constraints. However, the approximation often induces little performance degradation.

VI. SIMULATION RESULTS

In this section, to verify the effectiveness of the proposed DAP architecture, we evaluate the performance of spectrum efficiency as well as the energy efficiency compared with classical sub-connected hybrid precoding and classical fully-connected precoding algorithms. Moreover, we investigate the performance for different choices of data streams N_s in the near-field XL-MIMO communication systems.

In the simulations, we consider a single-user XL-MIMO communication scenario. Both the transmitter and receiver are equipped with ULA with 256 elements spacing of half wavelength. The carrier wave is set to 100 GHz, with wave length of $\lambda = 3$ mm. It can be calculated that the Rayleigh distance is around 100 m under the settings. The transmission distance varies within the Rayleigh distance in our simulations. For the wireless channel, as mentioned before, we adopt the deterministic LoS channel in (4) and assume that the large-scale channel fading can be ignored through perfect power control.

A. Evaluating the Performance of Spectrum Efficiency

The spectrum efficiency for the proposed DAP architecture over different distances is shown in Fig. 5. The SNR $= P_{\text{tot}}/\sigma_n^2$ is set to 30 dB. The baselines include fully-digital precoding, fully-connected hybrid precoding with 8, 4 RF chains using an alternating minimization algorithm [25], and sub-connected hybrid precoding with 8, 4 RF chains using the SIC-based algorithm [20]. When the transmitter-receiver distance is small, the proposed scheme can achieve about 40% increase in the achievable spectrum efficiency compared to classical hybrid precoding schemes with 8 RF chains. This is because the proposed architecture can benefit from the extra DoFs in the near-field region. When the transmitter-receiver distance grows, the fully-connected hybrid precoding outperforms our proposed architecture. The reason lies in that there still exists a gap between the fully-connected architecture and sub-connected architecture with the same number of RF chains, as illustrated in Section VI-C. When the transmitter-receiver distance grows larger, the DoFs reduce and our proposed architecture could no longer obtain the multiplexing gain from the extra RF chains.

Another simulation is carried out over different SNRs in Fig. 6. The SNR ranges from 20 dB to 30 dB. From Fig. 6, the proposed DAP architecture outperforms other precoding architectures with fixed RF chains.

B. Evaluating the Performance of Energy Efficiency

With the increasing N_s , the proposed DAP is approaching the classical fully-digital precoding scheme. The advantage of the DAP architecture lies in that it significantly increases

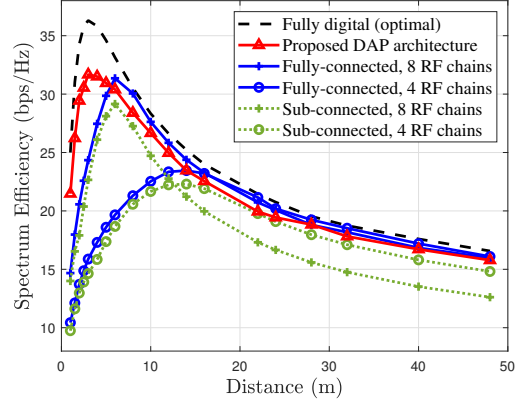


Fig. 5. The comparison of spectrum efficiency over different distances.

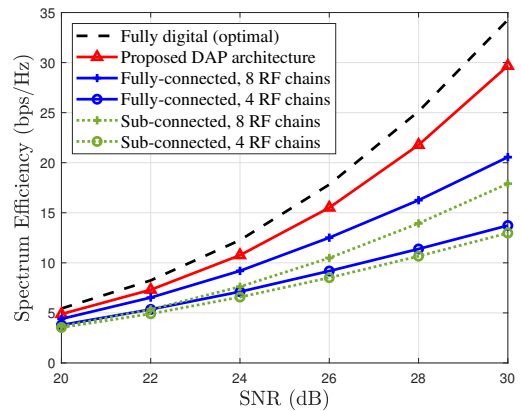


Fig. 6. The comparison of spectrum efficiency over different SNRs.

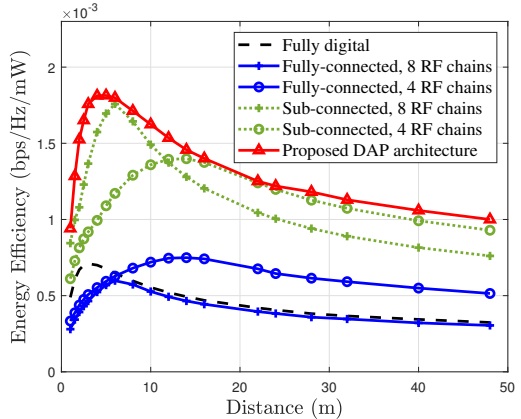


Fig. 7. The comparison of energy efficiency over different distances.

the spectrum efficiency utilizing the enlarging DoFs in the near-field region. Also, the scalable RF chains can match the DoFs to save unnecessary energy consumption. Therefore, another critical performance factor, energy efficiency, needs to be considered in the simulations. For simplicity, we claim a downlink power consumption model at the base station, and the energy efficiency can be formulated as

$$\eta = \frac{R}{P_T + N_s P_{\text{RF}} + N_{\text{PS}} P_{\text{PS}} + N_{\text{SW}} P_{\text{SW}} + N_t P_{\text{PA}}}, \quad (36)$$

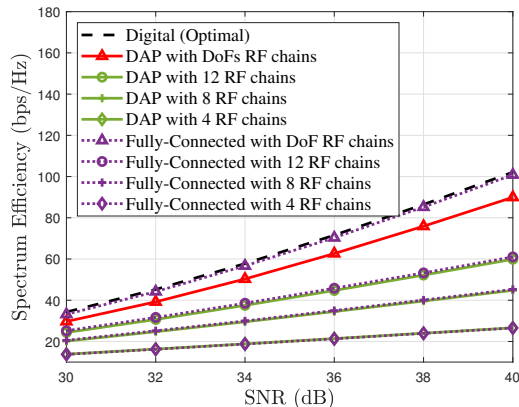
where P_T is the constant circuit power, P_{RF} , P_{PS} and P_{SW} denote the power consumption for each RF chain, phase shifter and switch respectively, N_{PS} and N_{SW} denote the number of phase shifters and switches respectively. $P_T = 2500$ mW, $P_{RF} = 160$ mW, $P_{PS} = 10$ mW, $P_{SW} = 10$ mW and $P_{PA} = 30$ mW are assumed. The baselines also include the fully-digital precoding, fully-connected and sub-connected hybrid precoding schemes. In fully-connected hybrid precoding architectures, the number of phase shifters is equal to $N_{PS}^{FC} = N_t N_{RF}$. While in sub-connected hybrid precoding architectures, the number of phase shifters equals to the number of antennas $N_{PS}^{SC} = N_t$. Classical fully-connected and sub-connected hybrid architectures are implemented without switches, while in the proposed DAP architectures $N_{SW} = N_s$. The simulation results of energy efficiency are shown in Fig. 7. We can observe from Fig. 7 that, the proposed DAP architecture also outperforms all other precoding architectures, which reveals the superiority of the proposed DAP architecture in terms of the energy consumption for transmitting the same amount of data.

C. Evaluating the Effect of Different N_s

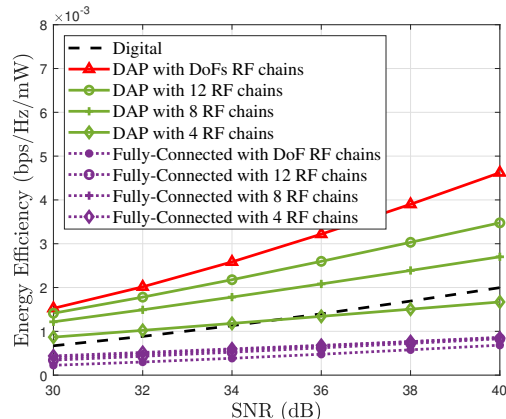
In the proposed DAP algorithm, we have assumed that N_s is equal to N_{DoF} . To verify the rationality of choice, we compare different choices of N_s with $N_s = N_{DoF}, 12, 8, 4$. The transmission distance is 2 m. The precoding baselines considered include the proposed DAP architecture and fully-connected precoding architecture with alternating precoding algorithm [25]. As shown in Fig. 8(a), the spectrum efficiency increases with increasing N_s . With different N_s , the performance of fully-connected precoding scheme outperforms our proposed sub-connected DAP architecture, which is consistent with previous works. When N_s is chosen to N_{DoF} , the fully-connected precoding scheme approaches the optimal fully-digital precoding scheme, which reveals that the choice of N_s can be considered optimal. It is worth noting that, there is still a gap between the fully-connected precoding and proposed sub-connected DAP precoding scheme. However, as illustrated in Fig. 8(b), the proposed DAP architecture with $N_s = N_{DoF}$ outperforms all other settings in terms of energy efficiency. Therefore, the proposed DAP architecture can achieve spectrum efficiency and energy efficiency improvements with N_s equal to N_{DoF} .

VII. CONCLUSIONS

In this paper, the significantly increased DoFs and the channel capacity in the near-field region are theoretically analyzed. To utilize the increased spatial DoFs, a DAP architecture and the corresponding precoding algorithm have been proposed for the XL-MIMO communication scenario, in which the number of activated RF chains can be flexibly adjusted to match the increased DoFs in the near-field region. Simulations results show that, compared with the classical sub-connected hybrid precoding architecture, the proposed DAP architecture can efficiently utilize the increased DoFs to significantly improve the spectrum efficiency in the near-field region. Different from alleviating problems brought by the near-field effect, this paper



(a) Spectrum efficiency



(b) Energy efficiency

Fig. 8. The comparison of different N_s over spectrum efficiency and energy efficiency. The number of RF chains is chosen within N_{DoF} , 12, 8, 4. The precoding architectures considered include fully-digital precoding architecture, proposed DAP architecture, fully-connected precoding architecture. The SNR varies from 30 dB to 40 dB.

has revealed that the near-field property can be exploited to improve the performance of XL-MIMO communications, which may provide another methodology to meet the increasing demand of communication capacity. Our future research will focus on the capacity enhancement employing reconfigurable intelligent surface (RIS) considering the near-field effect.

APPENDIX A

As shown in Fig. 1, according to the near-field channel in (4), the difference of the distance between j th and $(j+n)$ th transmitter antenna with i th receiver antenna is written as

$$r_{pq} - r_{p(q+n)} = r_{pq} \left(1 - \sqrt{1 + \left(\frac{nd}{r_{pq}}\right)^2 - 2\frac{nd}{r_{pq}} \sin \phi_{pq}} \right) \approx \overset{(a)}{nd \sin \phi_{pq}}, \quad (37)$$

where ϕ_{pq} denotes the azimuth angle between the p th receiver antenna and the q th transmitter antenna. Approximation (a) is derived based on the Taylor Series expansion that $\sqrt{1-x} \approx 1 - \frac{1}{2}x$ when $x = 2\frac{nd}{r_{ij}} \sin \phi_{ij}$ is small enough. The approximation holds when $r_{ij} \gg nd$, which means that

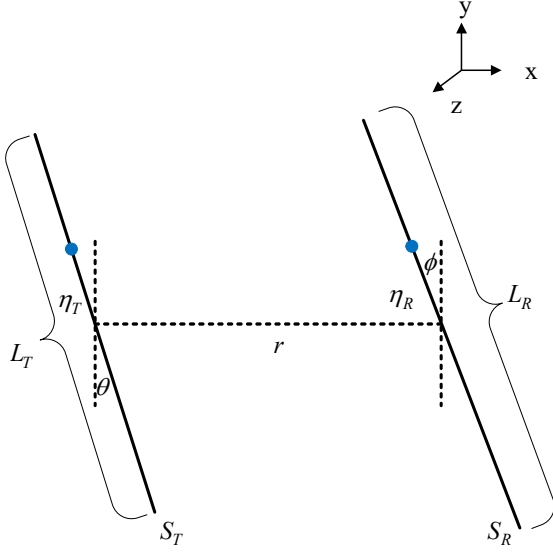


Fig. 9. Non-parallel continuous linear arrays in the near-field region.

the size of the receiver antenna can be neglected compared with the communication distance. In the far-field range, the azimuth of different elements and the normalized path loss in the same antenna can be regarded as the same. Then, the p^{th} row of \mathbf{H} can be approximated as

$$\mathbf{H}_{p,:} = \gamma_{\text{LoS}} \alpha e^{-j \frac{2\pi}{\lambda} r_{p1}} [1, e^{j \frac{2\pi}{\lambda} d \sin \phi_t}, \dots, e^{j(N_t-1) \frac{2\pi}{\lambda} d \sin \phi_t}], \quad (38)$$

where ϕ_t and ϕ_r represents the azimuth angle for all elements of the transmitter and receiver. The q^{th} column of \mathbf{H} can be formulated similarly. Thus, the near-field channel can be approximated as

$$\mathbf{H} = \gamma_{\text{LoS}} \alpha e^{-j \frac{2\pi}{\lambda} r_{11}} \mathbf{a}_r(\phi_r) \mathbf{a}_t(-\phi_t)^H. \quad (39)$$

Finally, by assuming $\alpha_{\text{LoS}} = \alpha e^{-j \frac{2\pi}{\lambda} r_{11}}$, $\phi_{\text{LoS}}^r = \phi_r$ and $\phi_{\text{LoS}}^t = -\phi_t$, the near-field LoS channel in (4) is degraded to LoS channel model in (2).

APPENDIX B

As shown in Fig. 9, we consider a pair of non-parallel continuous arrays in which the center of both transmitter and receiver are in the same horizontal line. The length of the transmitter and receiver is L_t and L_r respectively. And the slant angle for transmitter and receiver is θ and ϕ . Starting from the definition in (7), we aim to maximize the power of the derived wave function

$$\begin{aligned} |g|^2 &= \int_{S_R} \phi^*(\mathbf{r}_R) \phi(\mathbf{r}_R) d\mathbf{r}_R \\ &= \int_{S_R} \int_{S_T} \int_{S_T} G^*(\mathbf{r}_R, \mathbf{r}'_T) \psi^*(\mathbf{r}'_T) G(\mathbf{r}_R, \mathbf{r}_T) \\ &\quad \times \psi(\mathbf{r}_T) d\mathbf{r}'_T d\mathbf{r}_T d\mathbf{r}_R \\ &= \int_{S_T} \psi^*(\mathbf{r}'_T) \int_{S_T} K(\mathbf{r}'_T, \mathbf{r}_T) \psi(\mathbf{r}_T) d\mathbf{r}'_T d\mathbf{r}_T. \end{aligned} \quad (40)$$

Then, to maximize the value of $|g|^2$, $\psi(\mathbf{r}_T)$ has to be chosen as the eigenfunction corresponding to the largest eigenvalue [14]. The eigenfunction can be defined as

$$\begin{aligned} |g|^2 \psi(\mathbf{r}_T) &= \int_{S_T} K(\mathbf{r}'_T, \mathbf{r}_T) \psi(\mathbf{r}'_T) d\mathbf{r}'_T \\ &= \int_{S_T} \int_{S_R} \frac{\exp(jk|\mathbf{r}_R - \mathbf{r}_T|) \exp(-jk|\mathbf{r}_R - \mathbf{r}'_T|)}{(4\pi)^2 |\mathbf{r}_R - \mathbf{r}_T| |\mathbf{r}_R - \mathbf{r}'_T|} \\ &\quad \times d\mathbf{r}_R \psi(\mathbf{r}'_T) d\mathbf{r}'_T. \end{aligned} \quad (41)$$

It is worth noting that, the green function $G(\mathbf{r}_1, \mathbf{r}_2)$ is determined by the spherical wave assumption, which is also a basic assumption in the near-field communications. Then, since $|\mathbf{r}_R - \mathbf{r}_T| |\mathbf{r}_R - \mathbf{r}'_T|$ in the denominator is only a scalar factor, it can be viewed as r^2 if the transmission distance is relatively large. Then we concentrate on the nominator which contains a product of two phase items. Consider the variable η_t and η_r denote the distance from the center of transmitter and receiver respectively. Then we have

$$\begin{aligned} |\mathbf{r}_R - \mathbf{r}_T| &= \\ &= \sqrt{(r + \eta_T \sin \theta - \eta_R \sin \phi)^2 + (\eta_T \cos \theta - \eta_R \cos \phi)^2}. \end{aligned} \quad (42)$$

Here we adopt the paraxial assumption that the distance between the two arrays are relatively large compared with their apertures. The first three items in Taylor series $\sqrt{1+x} \approx 1 + \frac{1}{2}x - \frac{1}{8}x^2$ are adopted. Then we have

$$\begin{aligned} |\mathbf{r}_R - \mathbf{r}_T| &\approx r + \eta_T \sin \theta - \eta_R \sin \phi \\ &\quad + \frac{1}{2r} (\eta_T \cos \theta - \eta_R \cos \phi)^2. \end{aligned} \quad (43)$$

The product of the two phase items are formulated as

$$\begin{aligned} &\exp(jk|\mathbf{r}_R - \mathbf{r}_T|) \exp(-jk|\mathbf{r}_R - \mathbf{r}'_T|) \\ &= \exp \left\{ jk \left((\eta_T - \eta'_T) \sin \theta + \frac{\cos^2 \theta}{2r} (\eta_T^2 - \eta'^2_T) \right. \right. \\ &\quad \left. \left. - \frac{\cos \theta \cos \phi}{r} (\eta_T - \eta'_T) \eta_R \right) \right\}. \end{aligned} \quad (44)$$

We assume a focusing function as

$$F_T(\eta_T) = \exp \left\{ jk \left(\eta_T \sin \theta + \frac{\cos^2 \theta}{2r} \eta_T^2 \right) \right\}. \quad (45)$$

Then we have

$$\psi(\eta_T) = F_T(\eta_T) \alpha_T(\eta_T), \quad (46)$$

where $\alpha_T(\eta_T)$ are the solution of the formulation below

$$\begin{aligned} |g|^2 (4\pi r)^2 \alpha_T(\eta_T) &= \int_{-L_T/2}^{L_T/2} \int_{-L_R/2}^{L_R/2} \\ &\quad \exp \left\{ jk \frac{\cos \theta \cos \phi}{r} (\eta_T - \eta'_T) \eta_R \right\} d\eta_R \alpha_T(\eta'_T) d\eta'_T. \end{aligned} \quad (47)$$

It can be easily derived that the integral

$$\begin{aligned} &\int_{-L_R/2}^{L_R/2} \exp \left\{ jk \frac{\cos \theta \cos \phi}{r} (\eta_T - \eta'_T) \eta_R \right\} d\eta_R \\ &= \frac{\lambda r}{\cos \theta \cos \phi} \cdot \frac{\sin \Omega_T (\eta_T - \eta'_T)}{\pi (\eta_T - \eta'_T)}, \end{aligned} \quad (48)$$

where $\Omega_T = \frac{kL_R \cos \theta \cos \phi}{2r}$. Thus, the eigenfunction can be rewritten as

$$|g|^2 (4\pi r)^2 \alpha_T(\eta_T) = \int_{-L_T/2}^{L_T/2} \frac{\lambda r}{\cos \theta \cos \phi} \times \frac{\sin \Omega_T(\eta_T - \eta'_T)}{\pi(\eta_T - \eta'_T)} \alpha_T(\eta'_T) d\eta'_T. \quad (49)$$

Compared with the definition of prolate spheroidal wave functions in (9), parameter $c_y = \Omega_T \frac{L_T}{2} = \frac{\pi L_T L_R \cos \theta \cos \phi}{2\lambda r}$ is proportional to $\cos \theta \cos \phi$. Since N_{DoF} can be approximated as $N_{\text{DoF}} = \frac{2}{\pi} c_y$. Thus, the formulation in (12) can be obtained. Noting that the derivative process is under paraxial assumptions. When the arrays are non-parallel, the paraxial degeneracy will be removed, resulting different eigenvalues v_i in (9) when $i \leq \frac{2}{\pi} c_y$. However, since the eigenvalues v_i fall off rapidly in an exponential manner for $i > \frac{2}{\pi} c_y$, the DoFs still remain unchanged for θ and ϕ far smaller than $\pi/2$.

APPENDIX C

For a diagonal matrix \mathbf{F}_A and permutation matrix \mathbf{P}_S , since it has been proved that for any matrix \mathbf{A} , $\mathbf{B} = \mathbf{P}_S^T \mathbf{A} \mathbf{P}_S$ has the same diagonal entities as \mathbf{A} (but may with different orders) [26]. Thus, for any diagonal matrix \mathbf{F}_A , there exists a diagonal matrix $\tilde{\mathbf{F}}_A$ that has the same entities with \mathbf{F}_A subjecting to

$$\mathbf{F}_A \mathbf{P}_S = \mathbf{P}_S [\mathbf{P}_S^T \mathbf{F}_A \mathbf{P}_S] = \mathbf{P}_S \tilde{\mathbf{F}}_A.$$

Therefore, the order of the permutation matrix \mathbf{P}_S and diagonal analog precoder \mathbf{F}_A can be switched for further processings.

REFERENCES

- [1] S. Sun, T. S. Rappaport, R. W. Heath, A. Nix, and S. Rangan, "MIMO for millimeter-wave wireless communications: beamforming, spatial multiplexing, or both?" *IEEE Commun. Mag.*, vol. 52, no. 12, pp. 110–121, Dec. 2014.
- [2] E. Björnson, L. Sanguinetti, H. Wymeersch, J. Hoydis, and T. L. Marzetta, "Massive MIMO is a reality—what is next?: Five promising research directions for antenna arrays," *Digit. Signal Process.*, vol. 94, pp. 3–20, Nov. 2019.
- [3] O. Ayach, S. Rajagopal, S. Abu-Surra, Z. Pi, and R. W. Heath, "Spatially sparse precoding in millimeter wave MIMO systems," *IEEE Trans. Wireless Commun.*, vol. 13, no. 3, pp. 1499–1513, Jan. 2014.
- [4] J. Sherman, "Properties of focused apertures in the fresnel region," *IEEE Trans. Antennas Propag.*, vol. 10, no. 4, pp. 399–408, Jul. 1962.
- [5] M. Cui, L. Dai, R. Schober, and L. Hanzo, "Near-field wide-band beamforming for extremely large antenna array," *arXiv preprint arXiv:2109.10054*, Sep. 2021.
- [6] D. Headland, Y. Monnai, D. Abbott, C. Fumeaux, and W. Withayachumnankul, "Tutorial: Terahertz beamforming, from concepts to realizations," *APL Photon.*, vol. 3, no. 5, 2018, Art. No. 051101.
- [7] H. Zhang, N. Shlezinger, F. Guidi, D. Dardari, M. F. Imani, and Y. C. Eldar, "Beam focusing for near-field multi-user MIMO communications," *arXiv preprint arXiv:2105.13087*, May 2021.
- [8] M. Cui and L. Dai, "Channel estimation for extremely large-scale MIMO: Far-field or near-field?" *IEEE Trans. Commun. (early access)*, pp. 1–1, Jan. 2022.
- [9] Y. Han, S. Jin, C. Wen, and X. Ma, "Channel estimation for extremely large-scale massive MIMO systems," *IEEE Commun. Lett.*, vol. 9, no. 5, pp. 633–637, May 2020.
- [10] X. Wei and L. Dai, "Channel estimation for extremely large-scale massive MIMO: Far-field, near-field, or hybrid-field?" *IEEE Commun. Lett.*, vol. 26, no. 1, pp. 177–181, Jan. 2022.
- [11] Y. Han, S. Jin, C. Wen, and X. Ma, "Channel estimation for extremely large-scale massive MIMO systems," *IEEE Commun. Lett.*, vol. 9, no. 5, pp. 633–637, May 2020.
- [12] Z. Zhang and L. Dai, "Continuous-aperture MIMO for electromagnetic information theory," *arXiv preprint arXiv:2111.08630*, Nov. 2021.
- [13] D. Davide, "Communicating with large intelligent surfaces: Fundamental limits and models," *IEEE J. Sel. Areas Commun.*, vol. 38, no. 11, pp. 2526–2537, Nov. 2020.
- [14] D. A. B. Miller, "Communicating with waves between volumes: evaluating orthogonal spatial channels and limits on coupling strengths," *Appl. Opt.*, vol. 39, no. 11, pp. 1681–1699, Apr. 2000.
- [15] N. Decarli and D. Dardari, "Communication modes with large intelligent surfaces in the near field," *arXiv preprint arXiv:2108.10569*, Aug. 2021.
- [16] R. W. Heath, N. González-Prelcic, S. Rangan, W. Roh, and A. M. Sayeed, "An overview of signal processing techniques for millimeter wave MIMO systems," *IEEE J. Sel. Topics Signal Process.*, vol. 10, no. 3, pp. 436–453, Apr. 2016.
- [17] D. Slepian and H. O. Pollak, "Prolate spheroidal wave functions, fourier analysis and uncertainty — I," *The Bell System Technical Journal*, vol. 40, no. 1, pp. 43–63, Jan. 1961.
- [18] T. L. Marzetta and H. Q. Ngo, *Fundamentals of massive MIMO*. Cambridge University Press, 2016.
- [19] D. A. Miller, "Waves, modes, communications, and optics: a tutorial," *Adv. in Opt. and Photon.*, vol. 11, no. 3, pp. 679–825, Sep. 2019.
- [20] X. Gao, L. Dai, S. Han, C.-L. I, and R. W. Heath, "Energy-efficient hybrid analog and digital precoding for mmwave MIMO systems with large antenna arrays," *IEEE J. Sel. Areas Commun.*, vol. 34, no. 4, pp. 998–1009, Apr. 2016.
- [21] H. Wolkowicz and G. P. Styan, "Bounds for eigenvalues using traces," *Linear Algebra Appl.*, vol. 29, pp. 471–506, Feb. 1980.
- [22] Y. Sun, Z. Gao, H. Wang, and D. Wu, "Machine learning based hybrid precoding for mmwave MIMO-OFDM with dynamic subarray," in *Proc. IEEE Globecom Workshops (GC Wkshps)*, Dec. 2018, pp. 1–6.
- [23] S. Park, A. Alkhateeb, and R. W. Heath, "Dynamic subarrays for hybrid precoding in wideband mmwave MIMO systems," *IEEE Trans. Wireless Commun.*, vol. 16, no. 5, pp. 2907–2920, May 2017.
- [24] K. Xu, F. C. Zheng, P. Cao, H. Xu, and X. Zhu, "A low complexity greedy algorithm for dynamic subarrays in mmwave MIMO systems," in *Proc. IEEE 90th Veh. Technol. Conf. (IEEE VTC'19)*, Sep. 2019, pp. 1–5.
- [25] X. Yu, J. Z. J. Shen, and K. B. Letaief, "Alternating minimization algorithms for hybrid precoding in millimeter wave MIMO systems," *IEEE J. Sel. Areas Commun.*, vol. 10, no. 3, pp. 485–500, Apr. 2016.
- [26] J. Brewer, "Kronecker products and matrix calculus in system theory," *IEEE Trans. Circuits Syst.*, vol. 25, no. 9, pp. 772–781, Sep. 1978.